

# A CONTINENTAL RIFTING EVENT IN TANZANIA REVEALED BY ENVISAT AND ALOS INSAR OBSERVATIONS

A. M. Oyen<sup>1</sup>, P. S. Marinkovic<sup>1</sup>, C. Wauthier<sup>2,3</sup>, N. d'Oreye<sup>4</sup>, and R. F. Hanssen<sup>1</sup>

<sup>1</sup>*Delft Institute of Earth Observation and Space Systems, Delft University of Technology, Kluyverweg 1, 2629HS Delft, The Netherlands, A.M.Oyen@student.tudelft.nl, P.Marinkovic@tudelft.nl, R.F.Hanssen@tudelft.nl*

<sup>2</sup>*Royal Museum for Central Africa, Leuvensesteenweg 13, 3080 Tervuren, Belgium, c.wauthier@africamuseum.be*

<sup>3</sup>*Dept. ARGENCO, University of Liège, Sart Tilman B52, 4000 Liège, Belgium*

<sup>4</sup>*The National Museum of Natural History, Rue Josy Welter 19, 7256 Walferdange, G.D.-Luxemburg, ndo@ecgs.lu*

## ABSTRACT

From July to September 2007 a series of moderate earthquakes struck the area South of the Gelai volcano, located on the Eastern branch of the East African Rift (North Tanzania). Most deformation patterns detected by InSAR in these period are very complex, impeding proper interpretation. To decrease the complexity of the models of the deformation, this study proposes two strategies of combining data from different tracks and sensors. In a first stage a method is proposed to correct unwrapping errors in C-band using the much more coherent L-band data. Furthermore, a modeling optimization method is explored, which aims at the decomposition of the deformation in smaller temporal baselines, by means of creating new, artificial interferograms and the use of models. Due to the higher coherence level and fewer phase cycles in L-band, the deformation interpretation is facilitated but model residual interpretation has become more difficult compared to C-band.

Key words: East African Rift; continental rifting; radar interferometry; unwrapping; modeling.

## 1. INTRODUCTION

The East African rift (EAR) or the Great Rift Valley (see Fig. 1) is a linear, NNE-SSW oriented depression belt with volcanism and earthquakes all the way through the horn of Africa. However, the EAR does not coincide with a major plate boundary. The EAR is the result of continental stretching by the divergence of several parts of the African plate. More specifically for the Eastern branch of the EAR, the Nubian plate and Somalian plates, West and East of the EAR respectively, [7], are diverging. Many GPS studies were performed along the rift, [7] confirming the continental rifting processes, but except for Afar, [8], these deformations were not observed by InSAR so far.

This study makes use of both Envisat ASAR and

ALOS PalSAR radar images. Originally the project aimed at the monitoring of deformation of the Ol Doinyo Lengai volcano, located at the eastern branch of the EAR in Tanzania near the border of Kenya. During the seismic swarm of the period July–September 2007, large deformation patterns centered at the southern flank of the Gelai volcano were detected. The seismic swarm is recognized to be the consequence of a dyke intrusion south of the Gelai volcano, [4], [5]. This data set is quite unique because the continental rifting process is monitored from its very early stage.

Previous studies of these deformation patterns by C-band data showed that interpretation and proper modeling of the deformation were limited due to the low coherence on the dense vegetated flanks of the Gelai volcano and the dense fringe patterns in some of the interferograms, [5]. The ALOS satellite, which is launched in 2006, provides with its PalSAR instrument radar images in L-band (with single, dual or quad polarization). L-band interferograms show much higher coherence of the total scene and better penetration properties in the vegetated areas than radar interferometry in C-band, [9]. The large deformation patterns, centered at the dense vegetated Southern flank of the Gelai volcano, make it a perfect opportunity to combine Envisat and ALOS data. This work summarizes the development of two strategies of cross-combining data of different sensors and satellite tracks:

- The unwrapping improvement method aims at data combination of different sensors by means of data fusion. Two unwrapping improvement methods are proposed: one based on pixel substitution and one on ambiguity slip cycle detection.
- The modeling optimization method explores the possibilities of combining all possible data of a certain event in order to create artificial interferograms with decreased temporal baselines.

This paper is organized as follows. Section 2 reviews the available Envisat ASAR and ALOS PalSAR data and treats some critical steps in the L-band processing. The

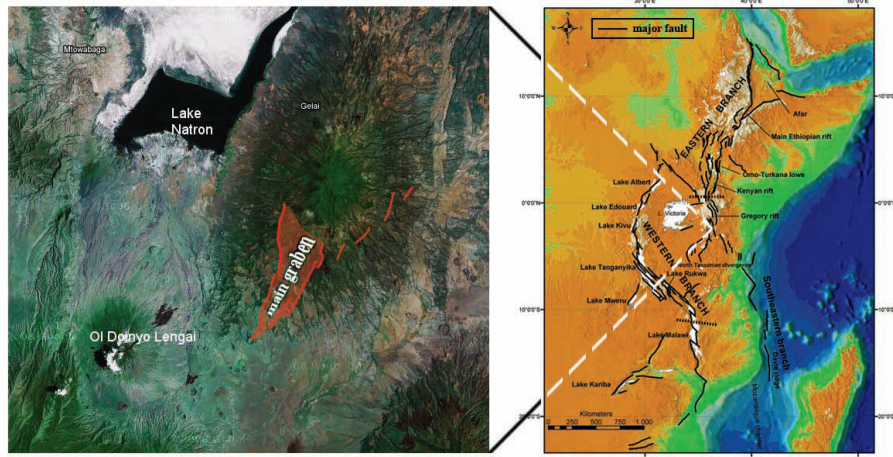


Figure 1. Overview of the East African Rift System and the main fault systems (right, Figure from [10]) and zoom on part of the Eastern branch of the East African Rift near the border of Tanzania and Kenya (left, screenshot from Google Earth). The red lines indicate surface ruptures detected by InSAR, the red colored part is the main graben.

two cross-combining methods, discussed in Section 3, will be applied on the Tanzanian seismic swarm in Section 4. Finally, in sections 5 and 6, the results are discussed and conclusions about C and L-band data combination are drawn.

## 2. DATA: AVAILABILITY AND INITIAL INTERPRETATION

The 2007 seismo-magmatic crisis in Tanzania was captured by Envisat ASAR as well as the ALOS PalSAR sensors. Images from three Envisat descending tracks were available, and are indicated by E(x-x); no ascending images were available as from 2006 because of Artemis failure at the equator. Furthermore, two image pairs (one descending and one ascending) of ALOS were available, which are indicated by A(x-x).

All the interferometric processing in the presented research has been performed with the DORIS InSAR processor [1]. However, ALOS SLC images, as distributed by ESA/JAXA, are focused in a so called “actual-Doppler” (AD) geometry, resulting in a skewed radar image, [6]; while for most of the other spaceborne SAR sensors the reference focusing geometry is a so called “zero-Doppler” (ZD) geometry. Moreover, in order to preserve the sensor’s ground resolution constant, the radar’s Pulse Repetition Frequency (PRF) is updated as a function of the sensor’s location/altitude. These PRF updates are performed autonomously by the PalSAR sensor itself.

These characteristics of ALOS/PALSAR data could lead to the potential problems in computing interferograms using the conventional InSAR processing algorithms. Namely, the problems in the coregistration procedure. Therefore, in order to account for the PRF difference and squint angle, two strategies for the optimization of the coregistration are devised: (1) deskewing of images before the coregistration procedure itself, (2) optimizations in the distribution of the correlation optimization win-

dows. Both of approaches are fully implemented and will be released in a new version of the DORIS software.

Focusing on the event, there are eight potential interesting interferograms. Fig. 4 shows a time line containing these interferograms. The dates of acquisition of master and slave images and other important parameters are indicated. To make Fig. 4 complete the larger than 5 Mw earthquakes are included (stars on the time line). More specifically, the largest shock that stroke on 17/07/2007 had a magnitude of 5.9 Mw and is called hereafter the main shock.

Based on the selected interferograms, the seismic swarm recorded South of the Gelai volcano is divided into three parts.

Part I contains the deformation before, during, and short after the main shock. This deformation is contained in interferograms 1:E(26613-28116), 2:E(25697-28202), and 3:A(07253-07924). Interferogram 4:E(28202-28703) covers Part II of the seismic swarm. In Part III deformation is detected on the eastern flank of the Gelai volcano only. This is shown in interferograms 7:E(28617-29619) and 8:E(28703-29204). Finally, interferograms 5:E(28116-28617) and 6:A(07727-09069), both having long temporal baselines, cover the first two and the three parts of the seismic swarm respectively.

The coherence images give, next to the fringe discontinuities in the wrapped interferograms themselves, important information about the appearance of surface ruptures. Examples are given in Fig. 2 and Fig. 3.

## 3. CROSS-COMBING DATA

This section describes two methods of how interferometric information of different wavelengths can be combined and integrated in order to extract the maximum amount of information. In order to combine data of different wavelengths and looking geometries, the interferograms are geocoded to the same reference frame and interpolated

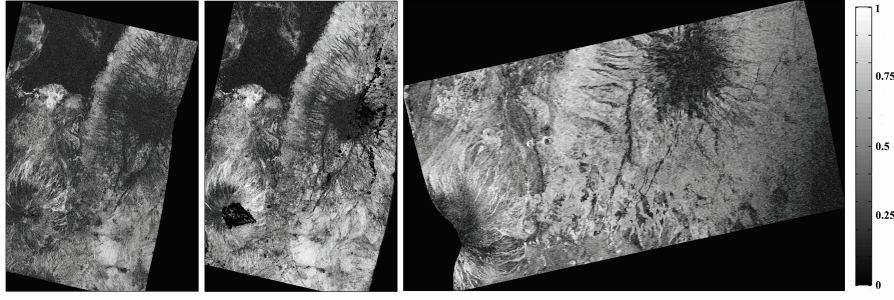


Figure 3. Coherence images of the 5:E(28116-28617) interferogram (left), the 4:E(28202-28703) interferogram (center), and 6:A(07727-09069) interferogram (right). Focusing on the surface ruptures, the 6:A(07727-09069) coherence image shows a much more detailed overview of those ruptures than the C-band interferograms.

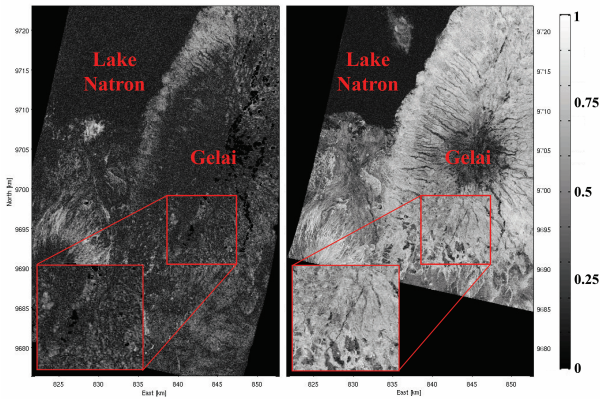


Figure 2. Coherence images of the 2:E(25697-28202) interferogram (left) and the 3:A(07253-07924) interferogram (right). The surface rupture, that is indicated by the red box, is created between 17/07/2007 and 21/07/2007 and is only detectable in the L-band interferogram.

onto a same grid.

The first method, studied in Subsection 3.1, focuses on the fusion of two interferograms with similar temporal baselines, but acquired at different wavelengths. More specifically, the L-band interferogram will be used as a-priori information in order to improve the unwrapping of the C-band one.

The second method, modeling optimization, addressed in Subsection 3.2, is applicable when several interferograms of complex deformation patterns are available. To understand the driving mechanisms behind those deformation patterns it is necessary to create a model of the deformation. When several ‘events’ occur in a short time span, these patterns can be very complex, which makes the modeling not straightforward. The modeling optimization method shows a strategy to create artificial interferograms with smaller temporal baselines utilizing models.

### 3.1. Unwrapping improvements by means of data fusion

Due to the higher overall coherence and less phase cycles in L-band interferograms compared to the C-band

ones (see Fig. 2 and Fig. 3) it is very likely that the L-band interferogram would contain fewer unwrapping errors. This is due to the higher noise levels in C than in L-band data. The data fusion method uses L-band data to improve the unwrapping of C-band interferograms. This improvement can be realized if both interferograms cover the same deformation, or the deformation can be assumed to be linear, and/or if deformation is known to be vertical (or horizontal).

Two potential unwrapping improvement methods will be explored here: low coherent pixel substitution and cycle slip detection.

Low coherent pixel substitution can be applied if both interferograms have similar look angles. Unwrapped values of low coherent pixels in one interferogram are substituted by the (rescaled, based on the temporal baseline and looking geometry differences) unwrapped value of the higher coherent pixel of the other interferogram.

The cycle slip detection method can be applied in two possible ways: ambiguity cycle slip adjustment (type I) and gradient optimization (type II):

- *Type I.* When ambiguity cycle slips are identified in certain regions of an interferogram, the integer ambiguity number and the location of the phase jumps, are estimated from a certain number of profiles taken perpendicular to the phase jumps. The estimation of the integer number is derived from the gradients along these profiles together with the estimated deformation from the wrapped interferogram and with the coherence.
- *Type II.* In case unwrapping errors are detected in the form of a more gradual, unlikely behaviour of the deformation that appears in the unwrapped profiles rather than interger ambiguity cycle slips, the gradient of the deformation along these profiles will be adjusted. In order to do this, the interferogram with the highest coherence and hence with the most reliable unwrapped values is utilized as a-priori information to constrain the gradient of the profiles in the less coherent, unwrapped interferogram.



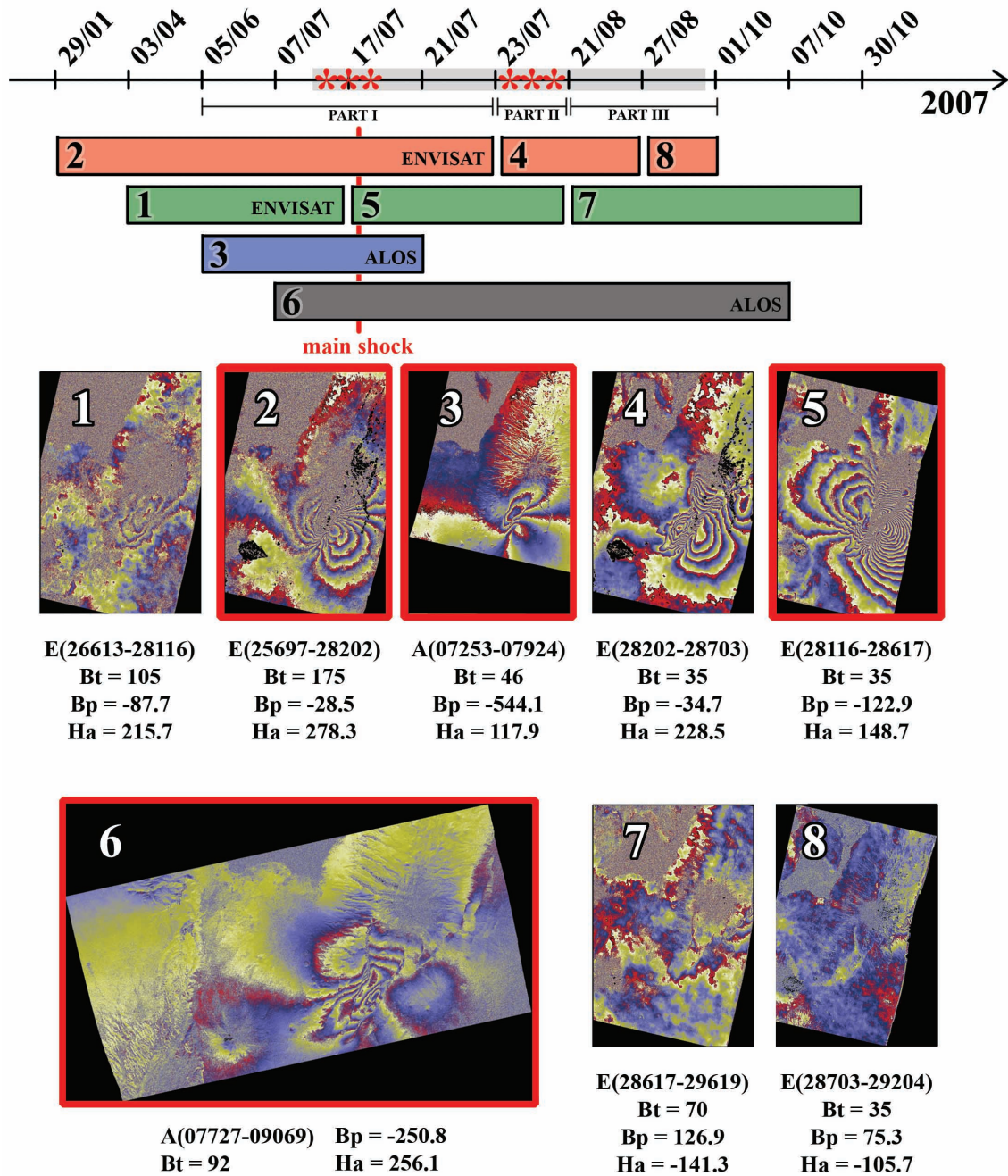


Figure 4. Summary of the differential interferometric results from 29/01/2007 to 30/10/2007. Green indicate the Envisat track 6 (swath is 6) interferograms, red the Envisat track 92 (swath is 2) interferograms. The descending and ascending ALOS interferograms are represented by blue and black respectively. Some important parameters of the interferograms, which are named by their respective orbit numbers, like temporal baseline ( $B_t$ ), perpendicular baseline ( $B_p$ ) and height ambiguity ( $H_a$ ) are listed next to each interferogram. The  $> 5$  Mw earthquakes of the seismic swarm, that started in the beginning of July 2007 and lasted up to September 2007, are indicated by the red stars on the time line. More specifically, the main shock is indicated by the vertical red line in the time line. The interferograms that contain this main shock are marked by the red boxes. The seismic swarm itself is indicated by the gray rectangle on the time line.



### 3.2. Modeling Optimization by means of Data Integration

When a certain area is struck by a series of earthquakes in a considerably small time span, the observed deformation in an interferogram did not occur gradually in time. In order to correctly interpret the deformation signal, as occurred during a seismic swarm (where earthquakes strike at a daily frequency), temporal baselines of interferograms are preferred to be as small as possible. Hence, deformation patterns can still be very complex, impeding the creation of realistic models, providing a good fit with the observations. Therefore, even the minimal temporal baseline of Envisat of 35 days, is too large to observe these kind of events. Hence, modeling and processing optimizations are needed.

When interferometric pairs of different tracks and sensors are available, consequently, the deformation is measured from different geometries and time spans. When these time spans overlap, it is desirable to make the use of, and to combine the deformation information from all the available interferograms. An example of such a combination is given by Fig. 5.

Due to differences in the observation geometry, interferograms cannot be directly subtracted from each other. To overcome this problem, the deformation modeling is not performed for every independent interferogram, but only for the parts of the total deformation signal. The proposed strategy is studied in more detail in Fig. 5. The modeling is performed by a 3D-MBEM (Mixed

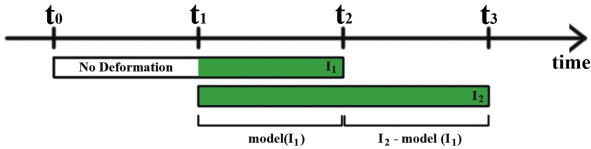


Figure 5. Sketch explaining the modeling optimization principle by means of two interferograms with different look geometries. The white color indicates a period without deformation between  $t_0$  and  $t_1$ , the green color indicates deformation between  $t_1$  and  $t_3$ . Interferogram  $I_1$  shows part of the deformation, while interferogram  $I_2$  captures the total deformation pattern. The modeled deformation in interferogram  $I_1$ ,  $model(I_1)$ , subtracted from interferogram  $I_2$  results in the deformation between  $t_2$  and  $t_3$ .

Boundary Element Method), [3], a mechanical model that considers topography and any type of sources to generate the deformation (fault planes, inflating/deflating sources, dyke intrusions). The method combines two boundary element methods: the direct method and the displacement discontinuity method. Furthermore it assumes a linearly elastic, homogeneous and isotropic medium. The elastic moduli are fixed at 5 GPa for Young's modulus and 0.25 for Poisson's ratio. The procedure starts with the meshing of the topography (e.g. using the SRTM DEM) of the area of interest. Then the sources have to be created by means of triangulation and put in the right position below the topography. The

inversion makes use of the neighborhood algorithm, [11], which searches regions in the parameter space that provide good data fits rather than looking for one single good fit. This case study makes use of the algorithm up to one single best fit model is found in the user-predefined parameter space.

## 4. CASE STUDY

The theory presented in Section 3 will be applied on the Tanzanian data set, which was reviewed in Section 2. The unwrapping improvement method will be applied to two interferograms acquired at different wavelengths with corresponding temporal baselines. The modeling optimization method will be applied on Part I of the seismic swarm. Also the application of the modeling optimization method on Part II will be discussed.

### 4.1. Unwrapping improvements by means of data fusion - the results

The strategies for unwrapping improvement are tested and validated on interferograms 3:A(07253-07924) and 2:E(25697-28202). Both interferograms cover the same major deformation pattern of Part I of the seismic swarm. Although seismic activity was observed between the slave images of both interferograms, for this optimization method, the deformation is assumed to be minor to that caused by the major earthquake on 17/07/2007.

Because of the large difference in look angles, which is approximately  $20^\circ$ , the low coherent pixel substitution method cannot be applied on these interferograms. Studying the full scene of the interferograms also no cycle slips of type I are detected. On the other hand, focusing more on the graben (see Fig. 6) and comparing the overall deformation patterns of both interferograms, the C-band interferogram seems to contain deformation which is unlikely with respect to the deformation observed in L-band. The unwrapped deformation inside the graben of the C-band interferogram will be corrected by means of the method presented in Subsection 3.1 concerning ambiguity cycle slips of type II.

Fig. 6 shows the results of the unwrapping optimization method by means of data fusion in the graben area. The validation of the Envisat unwrapping results is performed by cross-comparison of these results with interferograms containing the same deformation. The validation confirms that the unwrapping optimization is performed successfully.

### 4.2. Data integration - the results

As discussed in Section 2, the magmatic crisis in the Tanzanian EAR is split up in two main periods with magma intrusions. The modeling optimization method will be

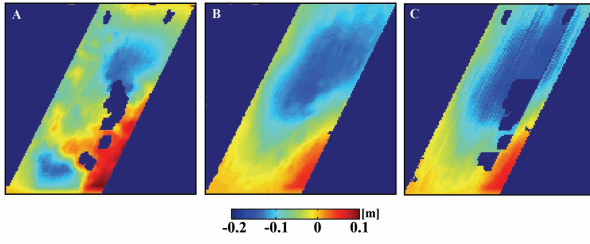


Figure 6. Unwrapped interferograms focused on the graben of the 2:E(25697-28202) interferogram (A) and the 3:A(07253-07924) interferogram (B). Due to the different looking geometries the unwrapped values in interferogram A should be consistent with the ones of interferogram B. Interferogram C shows the unwrapping optimization of interferogram A by means of the use of interferogram B as a-prior information. The black pixels are the geocoding artifacts.

applied on Part I and II of the seismic swarm, where the largest deformation patterns are detected.

### Part I

Part I of the crisis considers three interferograms having the following acquisition dates:

$t_0$ :	29/01/2007	$t_4$ :	17/07/2007
$t_1$ :	03/04/2007	$t_5$ :	21/07/2007
$t_3$ :	07/07/2007	$t_6$ :	23/07/2007

From other interferometric pairs appears that no deformation occurred before  $t_1$ . The deformation between  $t_1$  and  $t_4$  can be modeled by a buried, west-dipping normal fault (see Fig. 7). The model suggests an average slip on the fault plane of 1.0 m that corresponds to a moment magnitude of 5.23 Mw, which is close to the largest measured value of 5.4 Mw, [2]. It has to be mentioned, that this fault model represents all the deformation before 17/07/2007, and hence cannot be associated to one particular earthquake. Making the comparison of the cumulative seismic moment release before 17/07/2007 of  $6.5 \cdot 10^{16}$  N.m to that released by the model,  $8.9398 \cdot 10^{16}$  N.m, implying that 27% of the seismic moment is dissipated aseismically. When the modeled deformation of interferogram  $t_1 - t_4$  is subtracted from interferogram  $t_2 - t_5$ , the deformation between  $t_3$  and  $t_4$  remains. This is visualized by the dark blue part of the  $t_2 - t_5$  interferogram in the time line in Fig. 8. The residual deformation, representing the deformation between  $t_4$  and  $t_5$ , is modeled by: (i) a buried, west-dipping normal fault, corresponding to the main shock on 17/07/2007, and (ii) dyke intrusion with graben bounding faults from the top of the dyke up to the surface in the East and a smaller, blind one in the West. The average slip on the normal fault is 0.78 m corresponding to a seismic moment release of  $3.828 \cdot 10^{16}$ . The measured value is  $8.9125 \cdot 10^{17}$ , [2]. The maximum opening of the dyke is 1.46 m at a depth of 5 km below the Earth's surface. The graben bounding faults are modeled by applying a zero shear stress drop on the fault, or, in other words, as passive activated faults. This confirms they are triggered by the dike intrusion. At this stage the

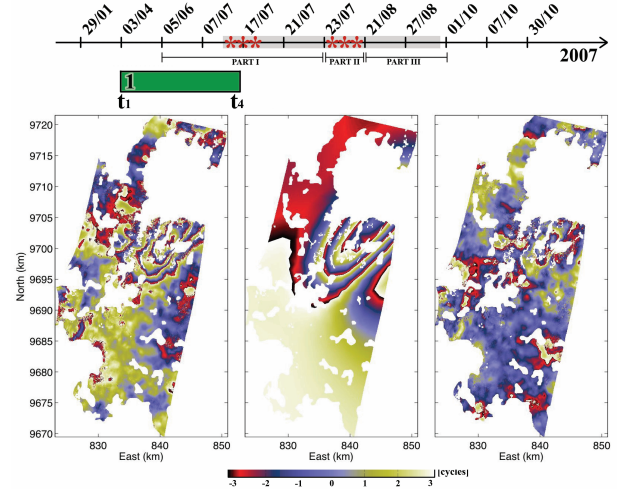


Figure 7. Interferogram 1:E(26613-28116) visualizes the deformation between  $t_1$  and  $t_4$ , represented by the green bar in the time line. The observed deformation is modeled by a blind, West-dipping normal fault. The model suggests a dip and strike angle of  $61^\circ$  and  $223^\circ$  respectively of the fault plane and an average slip of 1.0 m at 7 km below the Earth's surface. The residual deformation reveals that the model provides a good fit for 78% of the observed data. The RMS value is 1.07 cm.

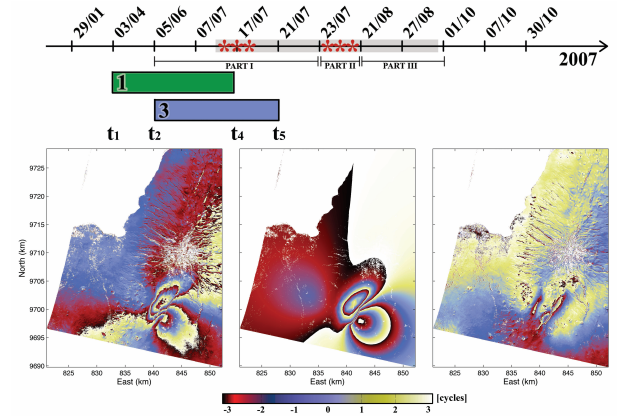


Figure 8. Left: Residual deformation after subtraction of the 1:E(26613-28116) model from the 3:A(07253-07924) interferogram, indicated by the dark blue bar in the time line. Center: Model of this residual deformation. Right: The residuals indicate that 80% of the observed deformation is estimated by the model. The RMS value is 3.11 cm.

deformation is explained up to 21/07/2007. The third interferogram that covers Part I of the seismic swarm shows also the deformation between  $t_4$  and  $t_5$ . The residual deformation if the  $t_1 - t_4$  and  $t_4 - t_5$  models are subtracted represents the deformation between 21/07/2007 and 23/07/2007, which is shown in Fig. 9.

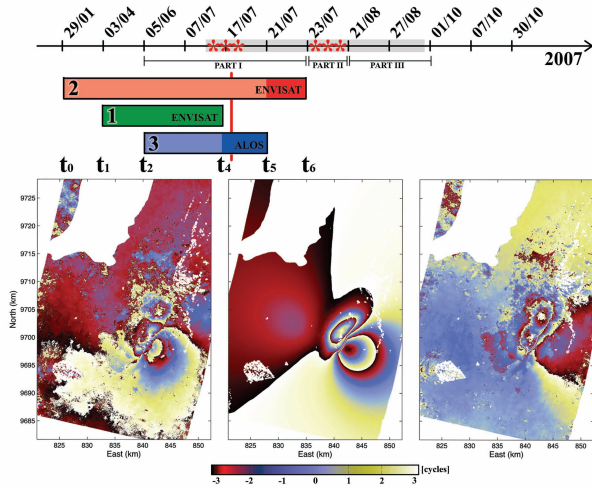


Figure 9. Residual deformation between the 2:E(25697-28202) interferogram ( $t_0 - t_6$ , red) and the  $t_1 - t_4$  (dark green) and  $t_3 - t_4$  (dark blue) models. This resulting signal (dark red) represents the deformation between  $t_5 - t_6$ . The residual range decrease inside the graben and range increase East of the graben indicate that the deformation between  $t_4$  and  $t_5$  is overestimated.

## Part II

There are two interferograms covering both magma intrusions, interferograms 5:E(28116-28617) and 6:A(07727-09069), and one interferogram covering only Part II of the crisis, namely 4:E(28202-28703). When the modeled deformation from 03/04/2007 till 23/07/2007 is subtracted from the 5:E(28116-28617) and 6:A(07727-09069) interferograms, the deformation caused by the second dyke intrusion period remains. Together with the 4:E(28202-28703) interferogram a well constrained model can be made of the dyke intrusion between 21/08/2007 and 27/08/2007.

Fig. 10 shows the three interferograms covering Part II of the seismic swarm. The residual deformation of interferogram 6:A(07727-09069) and the  $t_1 - t_4$  and  $t_4 - t_5$  models corresponds to the deformation in interferogram 4:E(28202-28703) and the residual deformation of interferogram 5:E(28116-28617) and the  $t_4 - t_5$  model.

Preliminary modeling of the three interferograms in Fig. 10 suggests (1) new dyke intrusions, (2) slip on graben bounding faults, (3) slip on a fault plane on the eastern flank of the Gelai volcano, and (4) that the fringes southwest of the graben are the result of slip on a fault plane.

## 5. DISCUSSION

The context of this study was to investigate and validate the performance of the proposed modeling and processing optimizations in terms of the modeling of the complex deformation signal. The initial validation showed promising results, however, the modeling itself needs to

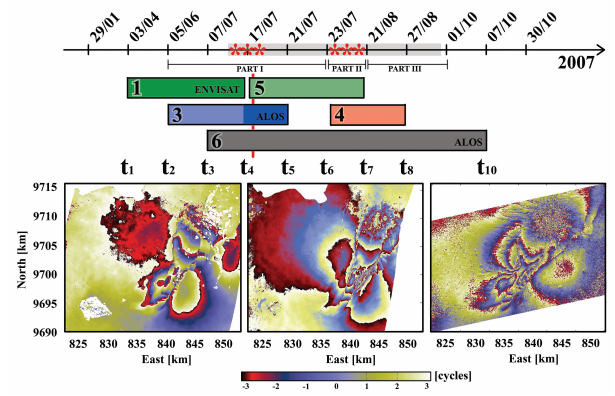


Figure 10. The three interferograms spanning Part II of the seismic swarm: Interferogram 4:E(28202-28703) rewrapped to L-band (left); the artificial interferogram, created out of interferogram 5:E(28116-28617) and ewrapped to L-band; and the artificial interferogram created out of interferogram 6:A(07727-09069) (right).

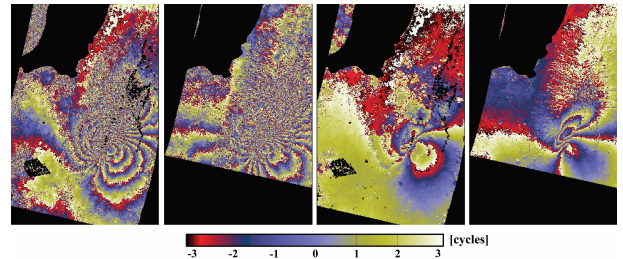


Figure 11. The two interferograms on the right show the 2:E(25697-28202) and 3:A(07253-07924) interferograms rewrapped to C. The two interferograms on the left show the same interferograms rewrapped to L-band. Notice the decrease of fringe density by a factor of four in the two interferograms on the left and the noise introduction in the second interferogram.

be further studied.

The presented study could be validated by the results obtained, by subtracting the  $t_4 - t_5$  model from interferograms 5:E(28116-28617) and 6:A(07727-09069), and comparing the fringe pattern with that of interferogram 4:E(28202-28703). Considering the difference in the interferograms' look geometries, deformation that does appear in artificial interferograms  $t_5 - t_7$  and  $t_5 - t_{10}$ , but not in the  $t_6 - t_8$  one, is likely to be the deformation that appeared between  $t_5$  and  $t_6$ . Through this procedure extra fringes are detected on both sides of the graben, indicating that between  $t_5$  and  $t_6$  the dyke intrusion propagated to the Northern part of the graben.

However, after applying the modeling optimization process on Part I, see Section 3.2, of the seismic swarm, the residual deformation does not confirm expectations. Fig. 9 indicates that the 3:A(07253-07924) modeling parameters are overestimating the observed signal. Two hypothesis for this residual (unmodeled) deformation could be drawn, either, the modeled deformation is overestimated by the  $t_4 - t_5$  model itself resulting in a few fringes of subsidence East of the graben in the residual deforma-



tion; and/or, this residual deformation can be explained by the increase of the noise level of C-band w.r.t L-band data, and by the lower deformation sensitivity of L-band. In principle, the wavelength of L-band results in a decrease of the number of fringes by a factor of four comparing to the C-band. This can be shown by rewrapping the L-band interferograms to C-band, and the other way around. To indicate this, two corresponding interferograms acquired in different wavelengths are rewrapped to C and L-band, showing that the rewrapping to L-band acts like a sort of a smoothing of the deformation and, hence, making the signal better interpretable, see Fig. 11. The introduction of noise when L-band interferograms are rewrapped to C-band, consequently, has an effect on the optimization strategies as presented in Subsection 3.2. When the smooth L-band model is subtracted from a C-band interferogram, errors in the model that seem to be negligible in L-band are introduced times a factor of four in C-band introducing extra signal instead of reducing it. Therefore, the modeling procedure has to be performed very accurately. This implies the need of very accurate models, which in their turn demand large CPU power and computing time.

## 6. CONCLUSIONS AND FUTURE WORK

In order to fully understand the deformation mechanisms of certain geophysical phenomena, the modeling of those phenomena is performed. Input for these models, could be different data sources, and in principle more data would (always) lead to the better model estimates. In case InSAR data would be used as an input for the modelling, usually only single sensor data (stacks) are utilized.

The primary objective of this study was to propose and validate strategies for a fusion of data obtained from different SAR sensors, for deformation modeling applications. More specifically, with this study, two strategies for integration of C and L-band data are presented. The first optimization is on the phase unwrapping algorithms, to account for noise / low coherence signal that would be potentially present in some interferograms. The second one, is the modeling optimization by means of the data fusion. Both proposed optimization strategies, have been applied successfully, tested and validated on the Tanzania data set.

Nevertheless, the initial results give a clear indication that combining the data of different wavelengths is very promising. However, in the case of the Tanzania data set, the resulting deformation patterns in the artificial interferograms with decreased temporal baselines are still very complex. This resulted in a situation that even though the number of model parameters is reduced, the number of assumptions, boundary conditions, and model uncertainties, that need to be accounted for in order to do a proper modeling, is relatively high. Consequently, this situation leads to a large computing power and processing time demands.

This potential drawback of modeling procedure is also

a part of the future work plans for this particular case study, through which the processing optimizations is intended in order to address such complex deformation models. Moreover, in terms of the unwrapping optimization strategies, future plans include the development of an automatic search algorithm for the unwrapping errors, which are at the moment implemented in a semi-manually manner.

## ACKNOWLEDGMENTS

The radar images presented in this study are captured in the frame of the ESA Cat-1 project CT-3224 and the ESA-JAXA ALOS project Nr 3690.

The authors would like to thank V. Cayol and Y. Fukushima for the use of the modeling scripts and helpful suggestions.

## REFERENCES

1. Delft object-oriented radar interferometric software (doris) - manual. Online: <http://enterprise.lr.tudelft.nl/doris>.
2. Usgs: United states geological survey. Online: <http://www.usgs.gov>.
3. V. Cayol and F.H. Cornet. 3d mixed boundary elements for elastostatic deformation fields analysis. *Int. J. Rock Mech. Min. Sci. and Geomech. Abstr.*, 24:275–287, 1996.
4. Baer et al. Evolution of magma-driven earthquake swarm and triggering of the nearby oldoinyo lengai eruption, as resolved by insar, ground observations and elastic modelubg, east african rift, 2007. *Earth and Planetary Science Letters*, 2008.
5. E. Calais et al. Aseismic strain accommodation by slow slip and dyking in a youthful continental rift, east africa. *Nature*, 2008.
6. Fornaro G. et al. Role of processing geometry in sar raw data focussing. *IEEE Transactions on Aerospace and Electronic Systems*, 38, 2002.
7. Stamps et al. A kinematic model for the east african rift. *Geophysical Research Letters*, 35, 2008.
8. Wright et al. Magma-maintained rift segmentation at continental rupture in the 2005 afar dyking episode. *Nature*, 442:291–294, 2006.
9. R.F. Hanssen. *Radar Interferometry. Data Interpretation and Error Analysis*. Kluwer Academic Publishers, Dordrecht, The Netherlands, 2001.
10. Chorowicz J. The east african rift system. *Journal of African Earth sciences*, 43:379–410, 2005.
11. Malcolm Sambridge. Geophysical inversion with a neighbourhood algorithm - i: Searching a parameter space. *Geophys. J. Int.*, 138:479–494, 1999.